FULL-FIELD STRAIN MEASUREMENT OF MATERIALS USING MESHLESS METHODS AND COMPUTER VISION

Giancarlo Gómez Gonzáles
Jaime Tupiassú Pinho de Castro
Marco Antonio Meggiolaro
Pontifical Catholic University of Rio de Janeiro, Department of Mechanical Engineering
Rua Marquês de São Vicente 225, Gávea. Rio de Janeiro, RJ – 22543-900
giancarlo.g.gonzales@hotmail.com
jtcastro@puc-rio.br
meggi@puc-rio.br

Abstract. *The objective of this work is to provide an experimental - numerical technique that combines the use of computer vision through the SIFT technique (Scale Invariant Features Transform) and meshless methods to determine displacement and strain fields on the surface of a deformable material. The experimental part of this technique is based on the capture of images during the deformation process of the material when it is subjected to mechanical forces. At this stage, the SIFT technique is used as an efficient filter for extraction and description of points with relevant characteristics in the images collected. For this purpose, the material surface was previously characterized using a local application technique that is able to generate points of interest which can be detected by the SIFT algorithm as potential keypoints. By tracking successfully matched SIFT points between two images, i.e. the reference image and the deformed image, it is possible to obtain the experimental displacement field. Finally, the application of the meshless formulation generates a numerical approximation for the displacement field and, therefore, the corresponding strain field can be estimated. Both solutions are built entirely in terms of these points provided by SIFT, called nodes. For this, the method of moving least squares is used. An experimental test is performed showing reliable results with good precision and robustness, proving to be a promising technique to further investigations in the field of structural mechanics.*

Keywords: SIFT, meshless methods, strain fields, moving least squares.

1. INTRODUCTION

Optical techniques have shown to be a powerful tool for the study of mechanical behavior of materials from full-field measurements of displacement and strain (i.e. constitutive laws, damage models, etc.). The main advantage is that the measurement does not interfere with the experimental process since there is no contact with the studied specimen.

Among several optical techniques, the Digital Image Correlation (DIC) (Sutton *et al*., 1983; Sutton, 2008) is the most widely used in the experimental mechanics area. Developed in the beginning of the 1980's, this technique has been improved for accuracy and reliability by many researchers over the years. The evolution of digital imaging introduced new modern methods of image processing and, consequently, the automation of the results.

The basic principle of DIC is to correlate two or more images of the material surface in different stages of mechanical deformation. In simple approaches, the DIC tracks the gray value pattern in small defined regions (called subsets) to locally obtain physical quantities such as displacement and deformation. In order to perform this process, a pattern with random characteristics on the specimen surface is required. Commonly, the correspondences between subsets in area-based techniques are defined by the normalized cross correlation (NCC), sum of squared differences (SSD), or variants of these methods.

Another approach for solving the correspondence problem is to extract features from the region of interest and use them to construct local image descriptors. Among feature-based techniques, one of the most robust in computer vision is the Scale Invariant Feature Transform (SIFT) proposed by Lowe (Lowe, 1999; Lowe, 2004).

The SIFT algorithm extracts characteristic points or features from images and further on constructs descriptors with invariant properties (e.g. scale, rotation, illumination and view point of camera). The SIFT features are highly distinctive, which allows them to be correctly matched with high probability against many features from different images. The matching process is based on similarity measures between descriptors, performed by computing the Euclidean distance.

This study proposes a methodology for full-field strain measurements incorporating the SIFT technique in the image correlation process. The SIFT algorithm automatically detects homologous features in the sequence of images recorded during mechanical testing. The nodal displacements are measured by tracking the positions of successfully matched keypoints in an undeformed-deformed pair of images. Then, the meshless approximation is used to define the continuous displacement field and its derivatives.

The meshless methods are mainly characterized by not requiring a mesh to represent the problem domain, depending exclusively on a set of nodes scattered within it. This flexibility permits that the matched SIFT keypoints are selected as nodes in a meshless formulation. Thus, the problems associated with mesh generation are eliminated.

Meshless approaches have been considerably improved in the last years (Liu, 2002). In this study, the element-free Galerkin method proposed by (Belytschko *et al*., 1994) is adopted, which uses the Moving Least Squares (MLS) procedure for the interpolation of the displacement function.

The main contribution of this work is to provide a new method for full-field displacement and strain measurement. The advantage of using SIFT descriptors lies on its robustness and automaticity in the matching process. These characteristics can be significant when compared with the area-based correlation techniques in order to analyze high strain gradients or large strain field measurement.

2. THE SCALE INVARIANT FEATURE TRANSFORM TECHNIQUE

The computation of the SIFT descriptor consists of the following four major steps (see Lowe D G, 1999 for details):

2.1 Scale-space extrema detection

In the first stage, the difference-of-Gaussian (DoG) operation is applied in various scales through the Gaussian pyramid. If the pixel represents a local maximum or minimum, it is selected as a candidate keypoint. As a result, these extracted points are invariant with respect to image scaling.

2.2 Keypoint localization and filtering

The final keypoints are selected based on measures of their stability. Unstable keypoints are rejected, which is decided by two criteria: the contrast level and the radius of principal curvature. If the computed values are below some threshold levels, the keypoint is kept, otherwise it is removed.

2.3 Orientation assignment

An orientation histogram is formed from the gradient magnitude and orientations of sample points within a region around the keypoint. Each keypoint will be assigned with a dominant orientation, allowing invariance with respect to image rotation.

2.4 Keypoint descriptor calculation

The local gradient data, calculated above, is also used to create keypoint descriptors. The gradient information is weighed by a Gaussian window with variance of 1.5 times the scale of the input. This data is then used to create a set of histograms over a window centered on the keypoint (Figure 1). The coordinates of the descriptor and the gradient orientations are rotated relative to the keypoint orientation to achieve orientation invariance. The descriptor is normalized to enhance invariance to changes in illumination.

Image gradients   Keypoint descriptor
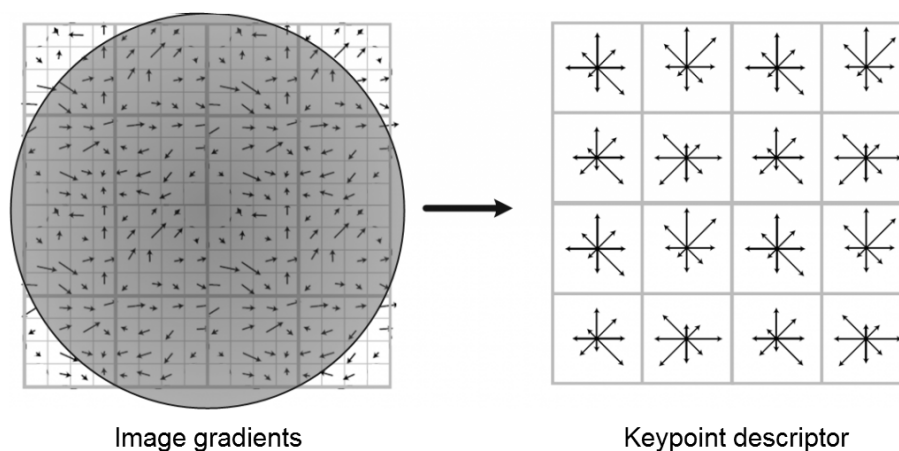
Figure 1. Keypoint descriptor computed from a set of 16 histograms in a 4x4 grid, each with 8 orientation bins. This leads in a feature vector containing 128 elements.

2.5 SIFT features matching

The best match for each descriptor is found by identifying its nearest neighbor (closest descriptor) in the database of keypoint descriptors from the captured images. In order to discard keypoints whose descriptors do not have any good match in the database, a subsequent threshold is used, which rejects matches that are too ambiguous. If the distance ratio between the closest neighbor and the second-closest neighbor is below some threshold, then the match is kept, otherwise the match is rejected and the keypoint is removed.

3. MESHLESS FORMULATION

In the meshless method, there is no direct connectivity between nodes, as opposed to the finite element method formulation, which connects them through the edges of the mesh. The connectivity between the nodes is given by the region of influence exerted by each node, called support domain (Figure 2). A support domain of an arbitrary point determines the number of nodes to be used to support or approximate the function value at this point.
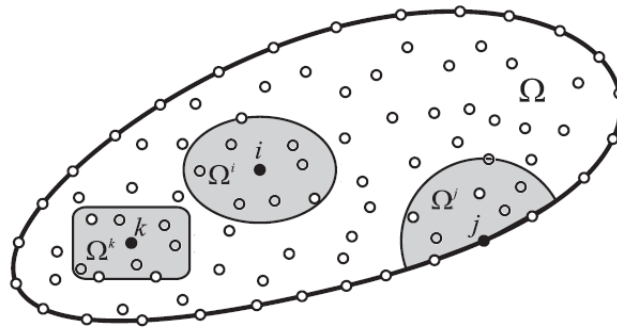

Figure 2. Example of different types of support domains. The figure shows the neighborhoods Ω_i, Ω_j to Ω_k and the nodes i, j and k, respectively.

The meshless approximation of the u-component of the displacement field at any point $\mathbf{x} = (x, y)$ is defined using the displacements at a finite set of nodes around it. These neighbor nodes constitute the support domain of point x, i.e.

$$u^h(\mathbf{x}) = \sum_{i}^{n} \phi_i(\mathbf{x}) u_i \tag{1}$$

where n is the number of nodes in the support domain of $\mathbf{x}$, ϕ_i is the shape function of the i-th node, and u_i the displacement of the i-th node.

3.1 MLS approximation

The MLS interpolation constructs shape functions to generate an approximating function obtained completely in terms of their adjacent neighboring nodes. The local approximation around a point $\mathbf{x}$ is defined in the domain Ω by (Belytschko *et al.*, 1994)

$$u_L^h(\mathbf{x}) = \sum_{i}^{m} p_i(\mathbf{x}) a_i(\mathbf{x}) \equiv \mathbf{p}^{\mathrm{T}}(\mathbf{x}) \mathbf{a}(\mathbf{x}) \tag{2}$$

where $\mathbf{p}^{\mathrm{T}}(\mathbf{x})$ is a linear polynomial basis of order m.

$$\mathbf{p}^{\mathrm{T}}(\mathbf{x}) = \left\{ 1 \quad x \quad y \quad xy \quad x^2 \quad y^2 \quad ... \quad x^m \quad y^m \right\} \tag{3}$$

The coefficients $\mathbf{a}(\mathbf{x})$ are obtained at a point $\mathbf{x}$ by minimizing the difference between the local approximation and the function, through

$$J = \sum_{i}^{n} w(\mathbf{x} - \mathbf{x_i})\left(u^h(\mathbf{x}) - u(\mathbf{x_i})\right)^2$$

$$= \sum_{i}^{n} w(\mathbf{x} - \mathbf{x_i})\left[\sum_{i}^{m} p_i(\mathbf{x})a_i(\mathbf{x}) - u_i\right]^2 \tag{4}$$

where $w(\mathbf{x} - \mathbf{x_i})$ is a weight function of compact support associated with each node .

The functional J can be minimized by setting the derivative of J with respect to $\mathbf{a}(\mathbf{x})$ equal to zero. The following linear relation between $\mathbf{a}(\mathbf{x})$ and $\mathbf{U}$ results:

$$\mathbf{a}(\mathbf{x}) = \mathbf{A^{-1}(x)B(x)U} \tag{5}$$

where

$$\mathbf{A(x)} = \sum_{i}^{n} w(\mathbf{x} - \mathbf{x}_i)\mathbf{p}(\mathbf{x}_i)\mathbf{p}^{\mathrm{T}}(\mathbf{x}_i) \tag{6}$$

$$\mathbf{B(x)} = w(\mathbf{x} - \mathbf{x}_i)\mathbf{p}^{\mathrm{T}}(\mathbf{x}_i) \tag{7}$$

$$\mathbf{U} = \sum_{i}^{n} u_i \tag{8}$$

Substituting Equation (5) into Equation (2),

$$u^h(\mathbf{x}) = \sum_{i}^{n}\sum_{j}^{m} p_j(\mathbf{x})\left[\mathbf{A}^{-1}(\mathbf{x})\mathbf{B}(\mathbf{x})\right]_{ji} u_i = \sum_{i}^{n} \phi_i(\mathbf{x})u_i \tag{9}$$

where, comparing with Equation (1), the shape functions $\phi_i(\mathbf{x})$ are obtained by

$$\phi_i(\mathbf{x}) = \sum_{i}^{n} p_j(\mathbf{x})\left(\mathbf{A}^{-1}(\mathbf{x})\mathbf{B}(\mathbf{x})\right)_{ji} \tag{10}$$

$$\phi_i(\mathbf{x}) = \mathbf{p}^{\mathrm{T}}\mathbf{A}^{-1}\mathbf{B}_i \tag{11}$$

The MLS shape function and their partial derivatives can be obtained from

$$\phi_i(\mathbf{x})_{,x} = \mathbf{p}^{\mathrm{T}}_{,x}\mathbf{A}^{-1}\mathbf{B}_i + \mathbf{p}^{\mathrm{T}}\mathbf{A}^{-1}_{,x}\mathbf{B}_i + \mathbf{p}^{\mathrm{T}}\mathbf{A}^{-1}\mathbf{B}_{i,x} \tag{12}$$

$$\phi_i(\mathbf{x})_{,y} = \mathbf{p}^{\mathrm{T}}_{,y}\mathbf{A}^{-1}\mathbf{B}_i + \mathbf{p}^{\mathrm{T}}\mathbf{A}^{-1}_{,y}\mathbf{B}_i + \mathbf{p}^{\mathrm{T}}\mathbf{A}^{-1}\mathbf{B}_{i,y} \tag{13}$$

where the subscript represents the spatial derivation.

Equation (1) can also be used for the displacement component $v(\mathbf{x})$, i.e.

$$v^h(\mathbf{x}) = \sum_{i}^{n} \phi_i(\mathbf{x})\mathrm{v}_i \tag{14}$$

The displacement field in the deformed surface is defined as

$$\begin{Bmatrix} u \\ v \end{Bmatrix}^h = \sum_{i}^{n} \begin{bmatrix} \phi_i & 0 \\ 0 & \phi_i \end{bmatrix} \begin{Bmatrix} u_i \\ v_i \end{Bmatrix} \tag{15}$$

Using Equation (12) and solving for *x* and *y*, the strain field is obtained by:

$$\begin{Bmatrix} \varepsilon_x \\ \varepsilon_y \\ \varepsilon_{xy} \end{Bmatrix}^h = \sum_{i}^{n} \begin{bmatrix} \dfrac{\delta}{\delta x} & 0 \\ 0 & \dfrac{\delta}{\delta y} \\ \dfrac{\delta}{\delta x} & \dfrac{\delta}{\delta y} \end{bmatrix} \begin{bmatrix} \phi_i & 0 \\ 0 & \phi_i \end{bmatrix} \begin{Bmatrix} u_i \\ v_i \end{Bmatrix} = \sum_{i}^{n} \begin{bmatrix} \phi_{i,x} & 0 \\ 0 & \phi_{i,y} \\ \phi_{i,x} & \phi_{i,y} \end{bmatrix} \begin{Bmatrix} u_i \\ v_i \end{Bmatrix} \tag{16}$$

Equations (15) and (16) are used to evaluate displacement and strain fields, respectively, for a given pair of undeformed-deformed images. All algorithms are integrated into a software program in the Matlab® environment (Mathworks, 2013), which facilitates the calculation of the solution.

4. EXPERIMENTAL SETUP

In order to demonstrate the performance of the proposed methodology, a four-point bending test is conducted with inner and outer spans of 80 mm and 118 mm, respectively (Figure 3). The experimental setup for the measurement of the full-field strain involves a load frame, a rectangular beam, a loading device, a stereoscopic vision system and a computer, as shown in Fig. 4. Table 1 contains the mechanical properties of the specimen used in this experiment.
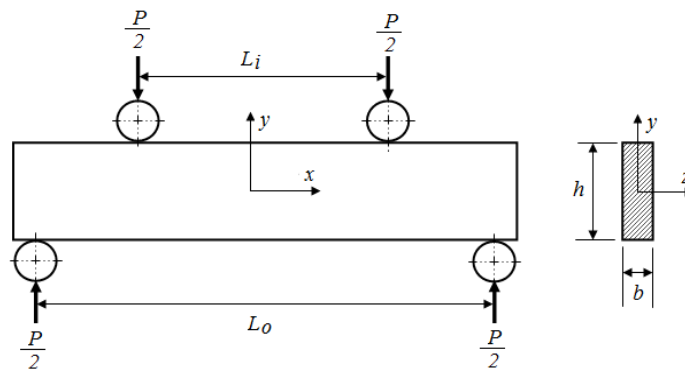

Figure 3. Scheme of the four-point bending test, where *h* = 20 mm, *b* = 11 mm, *L_i* the inner span distance and *L_o* the outer span distance.

Figure 4. Experimental setup.

Table 1. Mechanical properties of specimen.

Material	Polycarbonate
Young's modulus (E) [*]	2.4 GPa
Poisson's ratio (v) [*]	0.38

[*] experimentally measured in laboratory.

The image acquisition process is based on two synchronized CCD cameras observing the material surface during the experiment from different directions. In this case, the system is located on a fixed position, i.e. the calibration parameters are not changed during the performed mechanical test. Therefore, they can be determined through a stereo calibration as a preliminary step to system operation. The CCD cameras (*Point Grey GRAS-50S5M*) have a resolution of 2448×2048 pixels. In this experimental configuration, one pixel of the CCD camera corresponds to approximately 18.9 µm in the object plane.

The preparation of the specimen aims to provide a large number of possible points of interest that can be detected by the SIFT algorithm. For this purpose, the sample surface is covered with a uniform white acrylic paint and thereafter black dots are inserted by spray painting, see Fig. 5. The number of detected SIFT points inside the region of interest is particularly important, in order to obtain a reliable and precise measurement. The sprayed dots must cover densely the analyzed area and homogeneous patterns must be avoided.
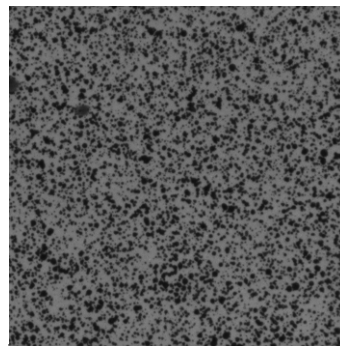

Figure 5. Surface detail of the specimen with painted speckles (random black and white pattern). The image corresponds to approximately 9.5×9.5 mm.

4.1 SIFT processing

The image captured with the specimen in the undeformed state is selected as the reference image. All the results have to be calculated with respect to this undeformed image, typically acquired in the beginning of the experiment. The deformed image is captured when a compression load of 100 N is applied. An area of interest (AOI) is then manually defined by the user, see Fig. 6. The SIFT algorithm works by first detecting a number of characteristic points in the reference image and in all the following captured images. The set of extracted keypoints are then matched using their SIFT descriptors.

The next step is computing the 3-D position of the set of matched keypoints. For this purpose, the matching process between each stereo-pair images provides the locations in the two views for the same keypoints, i.e., for a specific point in the left image, a unique point in the right image is identified as its corresponding one. Once both intrinsic and extrinsic parameters are known, one can solve the reconstruction problem unambiguously by a linear triangulation based approach. Thus, the displacement component in X-Y-Z directions for each matched keypoint can be computed by tracking the deformed and undeformed 3-D positions. This set of punctual displacement values represents the experimental displacement field of the material surface in the analyzed region. Table 2 shows a summary of the evaluation times for this analysis.

Table 2. Evaluation time for matching process.

Reference Image	10879 keypoints found
Deformed Image	10965 keypoints found
Matching process [*]	5846 keypoints found
Elapsed time[**]	120 seg

[*] Threshold value = 0.3
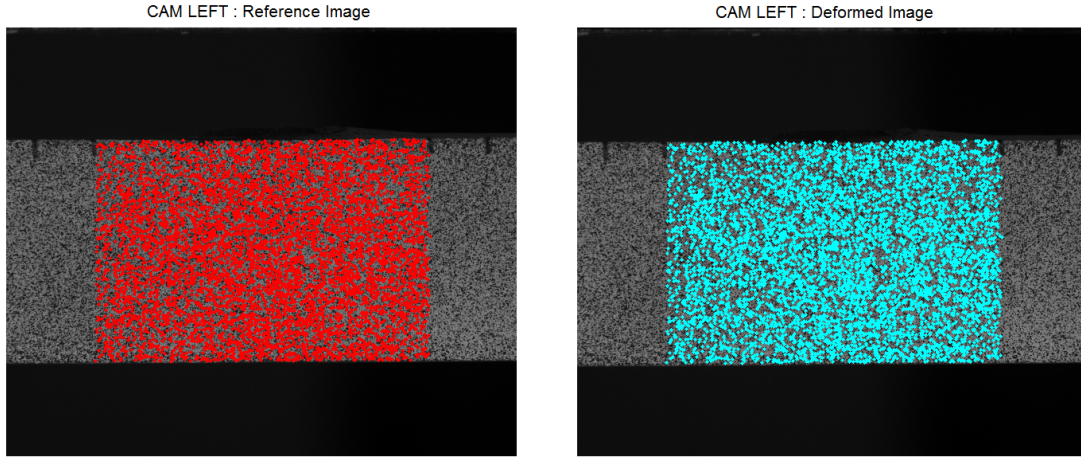[**] Intel core i7 processor at 2.2GHz.

Figure 6. The figure shows 5846 keypoints detected in a pair of undeformed (left) and deformed (right) images. The area of interest has approximately 1649×1110 pixels.

4.2 Meshless approximation

In this study, a circular domain is used containing a fixed minimum number of supporting points in the interpolation domain (see Fig. 7). The meshless approximation is constructed using an auxiliary grid of equally spaced nodes, spaced by 1 mm.
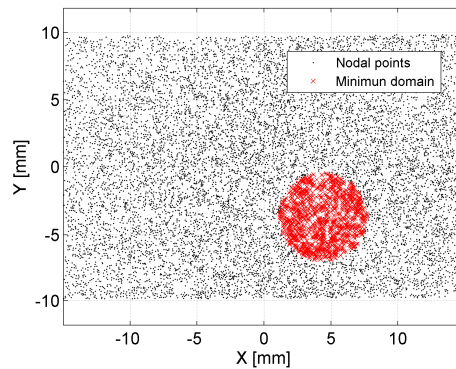

Figure 7. Circular domain with radius C_i for the neighborhood. The red area represents the dimension of the support domain used here, about 800 points.

The basis function, $\mathbf{p}^{\mathrm{T}}$, is defined in a two-dimensional domain by

$$\mathbf{p}^{\mathrm{T}}(x, y) = \left\{ 1 \quad x \quad y \quad xy \quad x^2 \quad y^2 \right\} \tag{17}$$

The Exponential weight function (Belytschko *et al.*, 1995) for a circular domain is applied, resulting in

$$w(\mathbf{x} - \mathbf{x}_i) \equiv w(r) = \begin{cases} e^{-(r/0.4)}, & |r| \leq 1 \\ 0, & |r| > 1 \end{cases} \tag{18}$$

where r is the support radius of node i. The dimension of r is calculated by the distance between the nodal point $\mathbf{x}_i$ and the point of interest $\mathbf{x}$ within the support domain of $\mathbf{x}_i$

$$r = \frac{\|\mathbf{x} - \mathbf{x}_i\|}{d_{mi}} \tag{19}$$

where d_{mi} is computed using a global support multiplier ($\alpha = 2$ to 4 led to good results):

$$d_{mi} = \alpha \cdot C_i \tag{20}$$

The table 3 shows a summary of the evaluation times for this analysis.

Table 3. Evaluation time for Meshless approximation.

Nodal points	5846
Grid points	600
Support domain	800
Elapsed time[*]	8.8 seg

[*] Intel core i7 processor 2.2GHz

5. RESULTS

The experimental strain fields obtained in the AOI for ε_x and ε_y are shown in the Fig. 8.
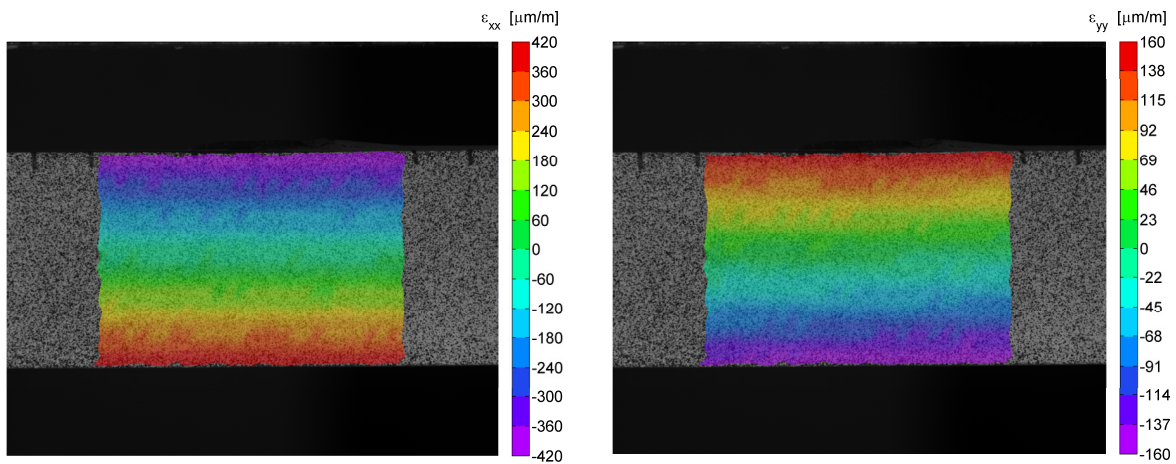

Figure 8. SIFT-Meshless full-field strain plot in *x* and *y* direction for the polycarbonate specimen under four-point bending.

The accuracy of the proposed algorithm is evaluated by checking the strain components at $x = 0$ against the expected solution using the FEM program ANSYS. In addition, measurements using the commercial digital image correlation system Vic-3D (Correlated Solutions, 2010) are also compared with the SIFT-Meshless results. The comparisons are presented in Fig. 9-10.
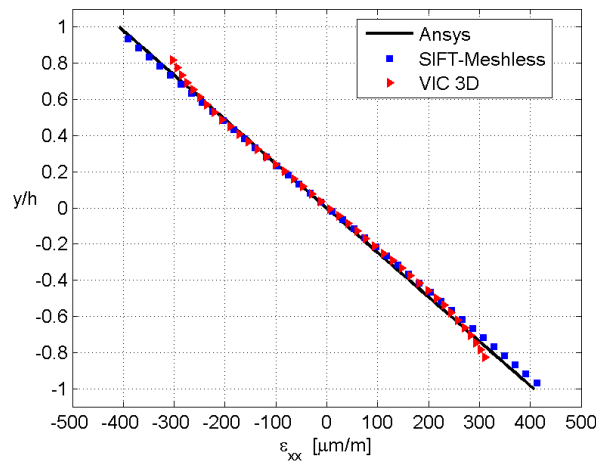

Figure 9. FEM, SIFT-Meshless, Vic-3D strain distributions at *x* = 0 for the ε_{xx} component.
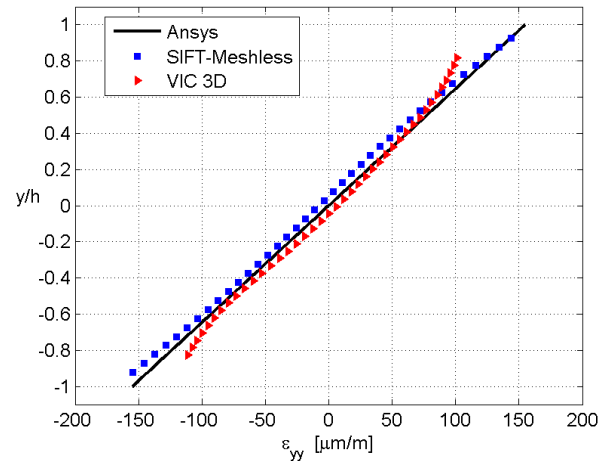
Figure 10. FEM, SIFT-Meshless, Vic-3D strain distributions at *x* =0 for the *ε*_{yy} component.

6. CONCLUDING REMARKS

The SIFT-Meshless technique described in this work has shown to be potentially useful for the determination of full-field strain fields. The experimental results have demonstrated that the proposed methodology can produce strain measurements without losing accuracy and with high reliability compared to other conventional DIC algorithms. The use of SIFT descriptors offers stable results for experimental displacement measurement by tracking detected keypoints in the captured images of the mechanical testing. The meshless formulation, based on the MLS approximation used here, ensures the continuity of the displacement field solution and its derivatives. For future works, the authors aim to approach the following problems: (i) three-dimensional strain measurements and (ii) strain concentration effects at notch roots under elastic-plastic conditions.

7. REFERENCES

Dolbow J. and Belytschko T., 1998. An introduction to programming the meshless element-free Galerkin method. Arch. Comput. Mech. Vol. 5, pp. 207–24.

Belytschko T., Lu, Y. Y. and Gu, L., 1994. Element free Galerkin methods. Int. J. Numer. Methods Eng. Vol. 37, pp. 229–256.

Belytschko T., Organ D. and Krongauz Y., 1995. A coupled finite element-element-free Galerkin method. Comput. Mech. Vol. 17, pp. 186–195.

Liu G. R., 2002, Mesh Free Methods: Moving Beyond the Finite Element Method. CRC Press.

Lowe D.G., 1999. Object recognition from local scale-invariant features. International Conference on Computer Vision, Corfu, Greece, pp. 1150-1157.

Lowe D.G., 2004. Distinctive image features from scale invariant key points. International Journal of Computer Vision, pp. 91-110.

Matlab, 2013, User Manual, Mathworks.

Sutton M. A., Wolters W. J., Peters W. H., Ranson W. F. and Mc Neill S. R., 1983. Determination of displacements using an improved digital correlation method, Image Vis. Comput. 1, Vol. 45, pp. 133–139.

Sutton M. A., 2008. Digital image correlation for shape and deformation measurements. Springer handbook of experimental solid mechanics. Berlin, Springer, pp.565–598.

Vic-3D, 2010, User Manual, Correlated Solutions.

8. RESPONSIBILITY NOTICE

The authors are the only responsible for the printed material included in this paper.